A microfluidic platform to investigate the role of mechanical constraints on tissue reorganization

S. Tlili, F. Graner, H. Delanoë-Ayari

00(00) 1–14

A microfluidic platform to investigate the role of mechanical constraints on tissue reorganization

Sham Tlili[1,2,c], François Graner[1] and Hélène Delanoë-Ayari[3]

[1]Laboratoire Matière et Systèmes Complexes, Université de Paris - Diderot, CNRS UMR 7057, Condorcet building, 10 rue Alice Domon et Léonie Duquet, F-75205 Paris Cedex 13, France
[2] Aix Marseille Université, CNRS UMR 7288, IBDM, Turing Center for Living Systems, Marseille, France
[3] Université Claude Bernard Lyon 1, CNRS UMR 5306, Institut Lumière Matière, Campus LyonTech - La Doua, Kastler building, 10 rue Ada Byron, F-69622 Villeurbanne Cedex, France
[c] sham.tlili@univ-amu.fr

Abstract Mechanical constraints have a high impact on development processes, and there is a need for new tools to investigate the role of mechanosensitive pathways in tissue reorganization during development. We present here experiments where embryonic cell aggregates are aspired through constrictions in microfluidic channels, generating heterogeneous flows and cell deformations that can be imaged using biphoton microscopy. This tool provides a way to measure *in situ* local viscoelastic properties of 3D tissues and connect them to intercellular and extracellular events such as cell shape changes and cell rearrangements. Perspectives include applications on organoids to investigate and quantify rheological properties of tissues, and to understand how constraints affect development.

Keywords : cell aggregates, tissue rheology, cell rearrangements, microfluidics, microscopy

1 Introduction

1.1 Motivation and state of the art

During embryo morphogenesis or wound healing, biological tissues are sculpted by active processes such as cell growth and division, cell migration or cell differentiation (1). These processes generate mechanical stresses within the tissue that can trigger tissue scale flows, cellular deformation and rearrangements. The nature of the tissue mechanical response to mechanical stresses depends on its rheological properties at the mesosopic scale, that of the group of cells. In turn, these mesoscopic properties arise from the microscopic interplay between cells viscoelasticity and cell-cell interactions such as adhesion.

To fully understand and measure these properties, 3D *in vitro* tissues such as cancer cell spheroids or embryonic organoids (2) play an increasingly important role in biophysical and medical studies as they are easy to handle and present very meaningful response and properties relevant for getting a better understanding of *in vivo* issues.

To study these *in vitro* tissue rheology in the context of developmental biology, several experimental setups have already been used, including cell monolayers stretching (3), rounding of cell aggregates (4–6), shearing of cell monolayers or cell aggregates (7–10), and compression of cell aggregates (5, 11, 12). These experiments have enabled to measure tissue bulk parameters such as shear and compression moduli, viscosity, surface tension and yield stress. To connect these bulk mechanical properties to cellular processes, it is essential to have access at the same time to the tissue micro-structure and to its dynamics (e.g. cell shapes or neighbour exchanges).

Live imaging in developing embryos and *in vitro* systems gives the opportunity to track cellular movements and divisions, cell shape variations and topological exchanges, and to quantify their contributions to the tissue scale dynamics, by measuring their contributions to the tissue strain rate for example (13, 14).

Methods combining the imposition of an external stress, force, strain or strain rate controlled by the experimenter with live imaging at a sub-cellular resolution have proven to be powerful approaches to investigate biological tissues and more generally complex materials rheological properties. For example, cell monolayers can be stretched by being suspended between rods or on an elastic membrane while imaging the tissue response at the cellular level (15, 16). Nanometric magnetic beads naturally endocytosed by the cells have also been used to apply a global force on cellular aggregates (12, 17).

A fruitful approach for 3D tissues is to embed ferro-magnetic droplets within the tissue which can be actively deformed by an externally applied magnetic field while imaging the tissue response at the cellular scale. This method has enabled to measure spatial gradients of yield stress leading to a jamming transition in the zebrafish mesoderm, and gives also access to the visco-elastic response of cells at short time scales (18). This approach provides a powerful method to probe locally tissue rheology at small deformation. To measure effective properties at large deformations, pipette aspiration are broadly used on 3D tissues such as cancer spheroids (9), embryos (e.g. mouse, xenopus (19), chicken (20)) and explants. However, it is not easy to image the tissue microstructure and its dynamical response in such aspirations geometries.

1.2 Approach and experiment principle

In this paper, we present a method to study 3D tissues mesoscopic mechanical properties and to relate these properties with microscopic structure such as cell shape and heterogeneities in cell proteins and gene expression. This approach is inspired from amorphous materials rheology (21, 22). Our method combines microfluidic aspirations with biphoton imaging of cell shapes at subcellular resolution. It enables to determine and correlate the spatiotemporal patterns of stresses generated within the tissue, the tissue-scale visco-elasto-plastic properties of 3D cell aggregates, and the cell-scale dynamics of cellular rearrangements.

The aspiration, forcing the aggregate to flow through a constriction, allows for an extensive control of tissue deformation. This geometry is interesting as it enables to apply a heterogeneous flow. As a consequence, each individual experiment provides a self-sufficient data set with a large enough variation range of cell deformations/tissue deformation rates. Moreover, this geometry enables to get large tissue deformations and to change tissue boundary conditions to probe tissue elastocapillary behaviour.

Imaging in 3D cell rearrangements and cell shapes is still challenging. To avoid technical difficulties of 3D analysis, we design a quasi-2D flow experiment (Fig. 1) where the tissue is physically constrained in the vertical dimension corresponding to the optical axis which forces it to flow in the plane of observation. We pre-confine the aggregate and use a capillary with straight sides (rather than a cylindrical pipette), thus creating a bidimensional flow (no dependency in z) that does not require 3D tissue reconstruction.

2 Material and Methods

2.1 Manipulation

For these experiments, we used mouse embryonic carcinoma F9 cell line (23). Aggregates were obtained resuspending single cells after trypsinization in a dish and preventing them to settle down using an orbital shaker. After two days we obtained aggregates with a diameter around 250 μm.

The experiment is performed on a microfluidic chip, Fig. 1a-c. The PDMS mold was obtained using standard lithography techniques. For the experiment presented here, the channel width was 50 μm and its height 100 μm. After bonding the PDMS chip to a glass coverslip using a plasma, we incubate the channel for 30 min with a pluronic solution in order to avoid the adhesion of the aggregate to the wall while flowing. It is then rinsed with Leibovitz complete medium, which was further used for the experiment. For the introduction of the aggregate we use a 200 μm cone, and the outlet is then linked to a fluid reservoir whose height can be adjusted in order to have a difference of pressure controlled by the difference in height in between the sample and the reservoir.

The aggregate is first dropped into a cone pipette. Then it sediments into a 100 μm high reservoir and deforms into a pancake shape (Fig. 1a-c). After waiting at least more than 10 minutes for stress relaxation, the aggregate is pushed towards the channel entrance. Because of the applied pressure difference, the aggregate slides into the reservoir towards the channel entrance and starts to deform inside the channel (Fig. 1d).

The aggregates were imaged on a two-photon inverted microscope using an oil immersion 40X objective (HCX PL APO CS 40.0x1.25 OIL UV) equipped with MaiTai Spectra Physics laser (690-1060 nm) used at 800 nm, and a lowpass filter below 600 nm, under a temperature control environment setup at 37°. To visualize the cell contours we used a solution of sulforhodamine B (5). We diluted 16 μl of a stock solution (1 mg/ml) in 1 ml of Leibovitz complete medium. With this method, bleaching is very low as the fluorophore rapidly diffuses from the medium to the extracellular space.

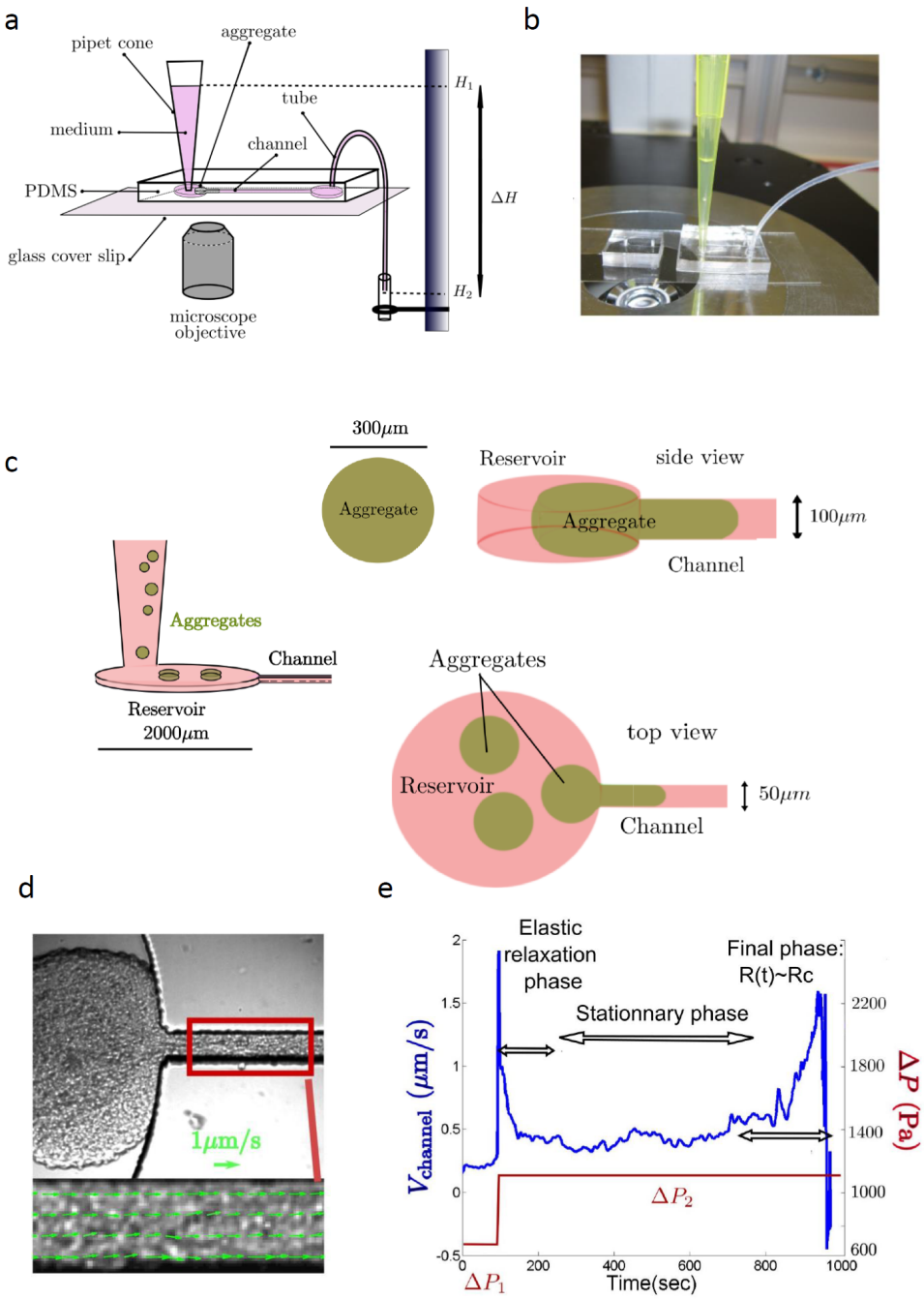

Figure 1: **Aggregate aspiration.** (a,b) Microfluidic device used to aspirate aggregates. Scheme and photograph of the device: a hydrostatic pressure difference is applied on the aggregate blocked inside the microfluidic channel. The microfluidic device is on a glass coverslip that allows imaging with an inverted microscope. (c) Microfluidic reservoir and channel top and side views. Preconfinement of the aggregate before aspiration: aggregates are put into the pipet cone, they sediment towards the channel reservoir. A pressure difference is applied inside the channel; the aggregate starts to enter into the reservoir and to deform in a pancake shape. (d) Brightfield image of an aggregate aspired in a channel (See Supplementary Movie 1). The red rectangle is the region used to quantify the flow rate. The inset shows the plug flow inside the channel which we could spatially average to obtain the mean velocity. (e) Aggregate flow rate inside the channel versus time.

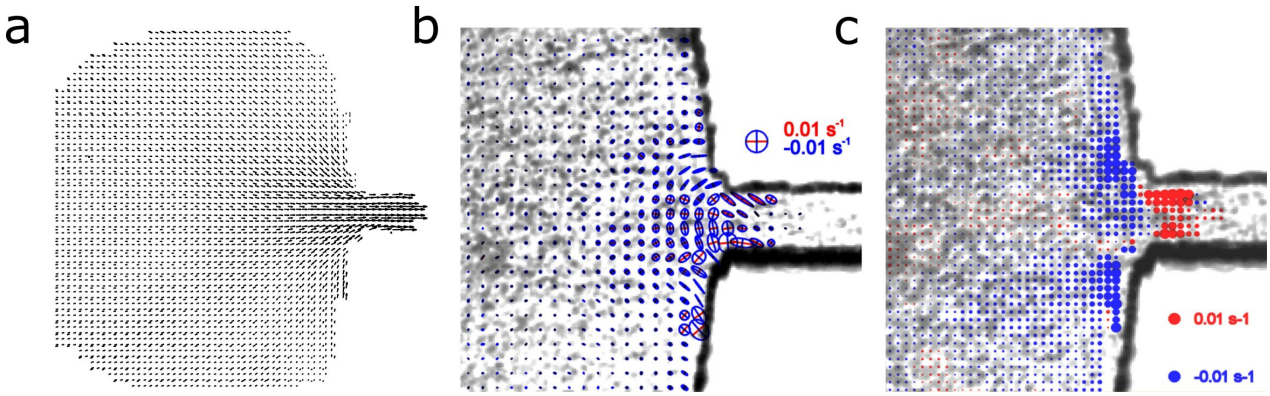

Figure 2: **Aspiration: maps of velocity and deformation.** (a) Time averaged velocity field over 5 min. (b) Tissue deformation rate corresponding to the previous velocity field. (c) Isotropic part of tissue deformation rate. (b) and (c) are overlayed with brightfield images.

2.2 Image analysis

We measure the two-dimensional velocity field $\vec{v}(x, y, t)$ using a custom-made Matlab optic flow code based on the Kanade-Lucas-Tomasi (KLT) algorithm (24) with a level 2 pyramid. This coarse-grained velocity field can be averaged in time, yielding components $v_i(x_j)$ where $i, j = 1$ or 2. Using finite differences we obtain in each box the symmetric part of the velocity gradient $\nabla \vec{v}_{\rm sym}$, with components $(\partial_i v_j + \partial_j v_i)/2$. This symmetric tensor can be diagonalized, we graphically represent in each box the tensors by ellipses whose axes and lengths correspond respectively to eigenvectors and eigenvalues with blue bars inside for compression and red bars for elongation.

To extract the coarse-grained cell anisotropy, we use Fourier Transform; details and validations are provided in (25). In short, the Fourier Transform of an image of a connective tissue has an ellipsoidal shape, whose axes and lengths give access to the average cell shape. This method provides an efficient measurement of the cell deformation field without having to recognize and segment each individual cell contour. We use the same grid and box size as for the velocity (box of 256 pixels, overlap 0.75).

We define as follows the cell shape deformation tensor $\varepsilon_{\mathbf{cell}}$ with respect to a rest state which we assume to be isotropic, with two equal eigenvalues $L_0 = (L_{\rm max} L_{\rm min})^{1/2}$. Hence $\varepsilon_{\mathbf{cell}}$ has the same eigenvectors as the Fourier pattern, and two eigenvalues $\frac{1}{2}\left(L_{\rm max}^2/L_0^2 - 1\right)$ and $\frac{1}{2}\left(L_{\rm min}^2/L_0^2 - 1\right)$. The deformation tensor $\varepsilon_{\mathbf{cell}}$ is equivalent to other definitions of the strain (e.g. true strain (25, 26)) within a linear approximation; in addition, $\varepsilon_{\mathbf{cell}}$ has the advantage to have well established transport equations (27).

We represent the deviator $\varepsilon_{\mathbf{cell}}^{\rm dev} = \varepsilon_{\mathbf{cell}} - {\rm Tr}(\varepsilon_{\mathbf{cell}}) I/2$, where I is the identity tensor: $\varepsilon_{\mathbf{cell}}^{\rm dev}$ is the anisotropic part of $\varepsilon_{\mathbf{cell}}$. It only depends on the ratio $\frac{L_{\rm max}}{L_{\rm min}}$, which are represented by ellipses whose color indicate the value of the deformation.

3 Results

3.1 Aspiration and brightfield microscopy

Here, we focus on macroscopic aspects of the flow properties in the aspired aggregate. Using brightfield or phase contrast microscopy gives already valuable information and enables to map the velocity field and tissue deformation rate in the aggregate. The velocity profile inside the channel is consistent with a plug-flow (Fig. 1d) and we integrate it over the channel cross-section to measure the aggregate flow rate. Over time, we observe three distinct phases of the aspiration (Fig. 1e): (i) a rapid elastic aspiration phase which corresponds to the rapid entrance through elastic cell deformation of the aggregate inside the channel; (ii) a stationary phase where the flow rate is rather constant, corresponding to an effective viscous behavior of the tissue; and (iii) a final phase of acceleration when the non-aspired aggregate part size is similar to the channel size, which indicates that the dissipation on the channel walls is negligible compared to the viscous dissipation inside the aggregate.

Taking advantage of the pseudo-2D flow structure, we quantify the in-plane spatial variation of the tissue flow/deformation rate within the aggregate (Fig. 2a). Models (9) predict that in a pipette experiment, the dissipation occurs only in a typical volume of effective radius $R_{channel}$. In our setup, we can have a spatially resolved measurement of the deformation rate: in our geometry, the typical size of the dissipation zone is similar to $R_{channel}$, but we observe an extended zone along the

walls of the chamber. We then measure the velocity gradient (Fig. 2b). The isotropic component of the tissue deformation rate (Fig. 2c) shows a compression against the walls before the channel entrance and an expansion after the entrance of the channel, which illustrates tissue compressibility.

3.2 Cell deformations and rearrangements during aspiration

To investigate the link between the material properties and the cellular dynamics, we image the tissue at the cellular scale to measure cell deformation (See Supplementary Movie 2). Here we use the same formalism that we used previously on a 2D system (MDCK monolayers (28)). Cell divisions can be neglected when they are inhibited, or when the timescale of the experiment $T_{\rm exp}$ is much smaller than the timescale of cell cycle $T_{\rm div}$; this is the case here, where $T_{\rm exp} \approx 1$ hour while $T_{\rm div} \approx 12$ hours. Then the total deformation rate $\dot{\varepsilon}_{tot}$ is the sum of the cellular deformation rate $\dot{\varepsilon}_{cell}$ and plasticity rate related to the rearrangement rate $\dot{\varepsilon}_r$.

We image at sub-cellular resolution the process of aspiration and observe simultaneously the heterogeneous velocity and deformation fields (Fig. 3a). The cell deformation pattern is due to the balance between: (i) the deformation induced by the constriction (i.e. the source term $\nabla\vec{v}_{\rm sym}$); (ii) the relaxation of cell deformation due to cell rearrangements ($\dot{\varepsilon}_r$); and (iii) elasticity transport terms (i.e. the fact that non-deformed cells are constantly advected towards the channel). We want to estimate the effective viscoelastic relaxation time related to cell rearrangements $\tau_{\rm relax}$, which can be defined as $\dot{\varepsilon}_{\rm r} \approx \frac{\varepsilon_{cell}^{\rm dev}}{\tau_{\rm relax}}$ where the superscript $\rm dev$ indicates the deviatoric (i.e. anisotropic) part of a tensor.

To take into account the transport of cell elasticity in the evolution of cell deformation, we measure the spatially averaged cell deformation $\langle\varepsilon_{cell}^{\rm dev}\rangle_{\rm box}$ and the deformation rate $\langle\nabla\vec{v}_{\rm sym}\rangle_{\rm box}$ in a Lagrangian box advected and deformed by the tissue flow (Fig. 3b). We can thus evaluate the terms of the evolution equation :

$$\langle\dot{\varepsilon}_{cell}^{\rm dev}\rangle_{\rm box} = \langle\vec{\nabla}\vec{v}_{\rm sym}^{\rm dev}\rangle_{\rm box} - \frac{\langle\varepsilon_{cell}^{\rm dev}\rangle_{\rm box}}{\tau_{\rm relax}} \tag{1}$$

We can measure at each timepoint the box-averaged tensors $\langle\varepsilon_{cell}\rangle_{\rm box}$ and $\langle\vec{\nabla}\vec{v}_{\rm sym}\rangle_{\rm box}$. We also simulate the possible evolutions of $\langle\varepsilon_{cell}\rangle_{\rm box}$ by injecting in Eq. 1 the experimental value of $\vec{\nabla}\vec{v}_{\rm sym}$ and by varying the parameter $\tau_{\rm relax}$.

We compare the simulated $\langle\varepsilon_{cell}\rangle_{\rm box}$ to the experimentally measured one. In Fig. 3c, we vary $\tau_{\rm relax}$ between infinity (purely elastic case in black) and 10 minutes. We obtain a reasonable agreement with the experimentally measured $\langle\varepsilon_{cell}\rangle_{\rm box}$ (red curve) when we use $\tau_{\rm relax} \approx 20$ min (gray curve). This relaxation time value is of same order of magnitude than the one we found for MDCK cells in a 2D migration experiment of cells around an obstacle: $\tau \approx 70$min (28). Assuming that the effective viscosity due to rearrangements is $\eta_{\rm T1} \approx G_{\rm tissue}\tau_{\rm relax}$, if we take at aggregate scale $\eta_{\rm T1} \approx 10^5$ Pa.s as we found previously (5, 8), we find $G \approx 100$ Pa, which is compatible with single cells rheological measurements performed on F9 cells (29).

Thus measurements coarse-grained at the level of the group of cells yield an estimate of an effective cell deformation relaxation time. Since divisions play a negligible role on the experiment timescale, the effective cell deformation relaxation time is necessarily associated with dynamics of cell rearrangements, which are numerous in particular near the constriction entrance (Fig. 3d).

3.3 Cell rearrangements dynamics

Using the same data, but at cell scale, we have access to the cell rearrangements dynamics at the scale of a single event (Fig. 4a) by manually identifying and segmenting cell-cell contacts which are disappearing and newly created.

As the deformation rate and cell deformation fields are heterogeneous, we can trigger in the same experiment: (i) "quasi-static" rearrangements in deformed regions of the tissue away from the channel, where both a disappearing link between cells losing contact and a newly appearing link between cells gaining a new contact can be clearly identified; and (ii) "sliding" rearrangements at the vicinity of the channel, where cells are highly stretched and flowing rapidly and seem to slide on each other. In the first case where rearrangements can be clearly identified and well-defined, we manually measured the disappearing and appearing junction lengths versus time (Fig. 4b). We define velocities of appearance and disappearance before and after the rearrangement, by taking the tangent of the junction lengths curves before and after the four-fold vertex stage. To have a robust definition, we define the velocity of disappearance $V^- = L^-(t=-T)/T$ and of creation $V^+ = L^+(t=+T)/T$ with $T = 6$ min. Their values are unchanged if we take $T \sim 10$ min, as the length evolution is locally linear around the four-fold vertex stage: we often see an asymmetry in V^+ and V^-.

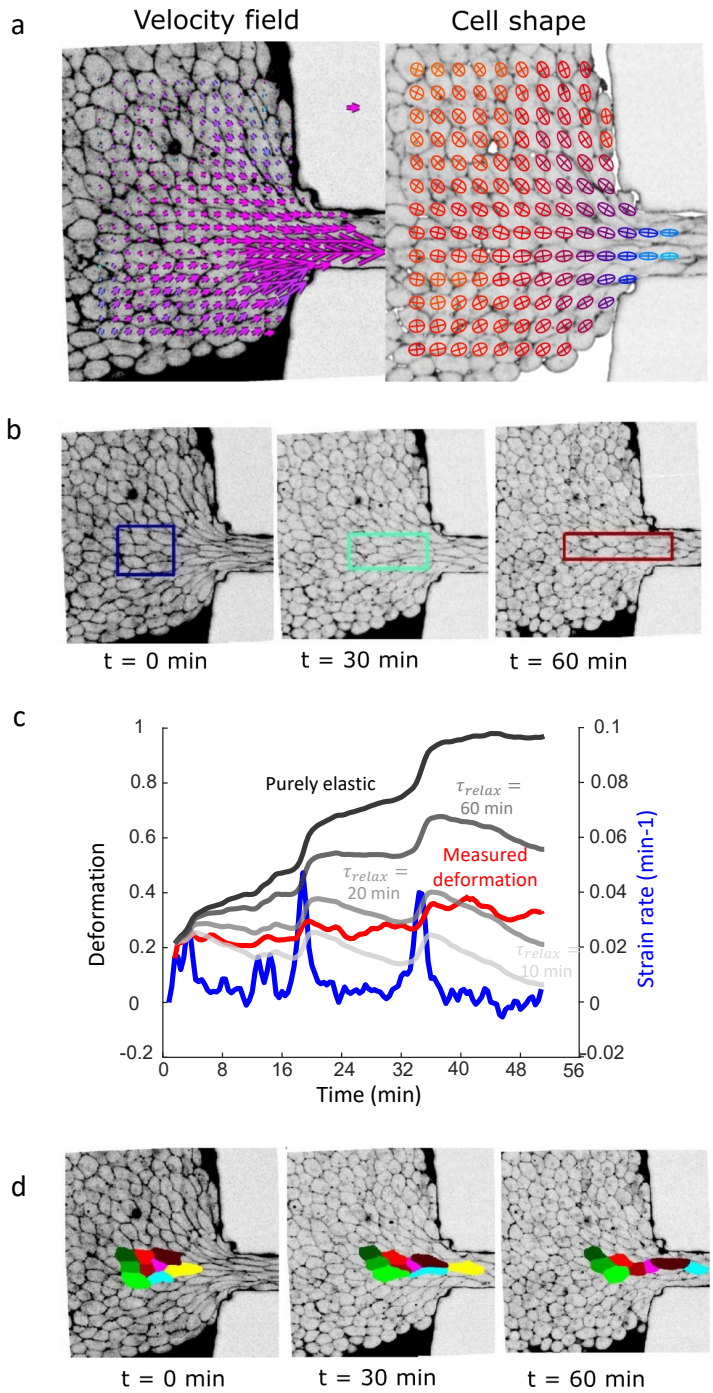

Figure 3: **Quantifying cell shape changes and relaxation during the aspiration**. The aggregate is imaged with an inverted two-photon microscope. (a) The optic flow method and Fourier transform method are performed on the cell contours (visible with the SRB dye) to measure the velocity field (on the left, average over 5 minutes), and the inertia ellipses representative of cell anisotropy (on the right, average over 5 minutes). Anisotropy is color-coded from 1 (red) to 3 (blue). (b) Virtual patch of tissue deformed and advected by the measured deformation rate/velocity field measured by optic flow. This patch is used to spatially average the tensors in the following analysis. (c) Estimation of the relaxation time τ. In the following, we plot the xx component of the anisotropic part of tensors T denoted as T^{xx-yy} spatially averaged in the deformed virtual tissue patch (lagrangian approach). In blue, $\dot{\varepsilon}_{\text{tot}}^{xx-yy}$, in red $\varepsilon_{\text{cell}}^{xx-yy}$, in black, simulated $\varepsilon_{\text{cell}}^{xx-yy}$ if there was no cell shape relaxation (purely elastic deformation), in gray levels, simulated $\varepsilon_{\text{cell}}^{xx-yy}$ in the case of a typical cell shape relaxation timescale τ_{relax}. (d) Tracking of a group of cells in the virtual patch and identification of cell rearrangements.

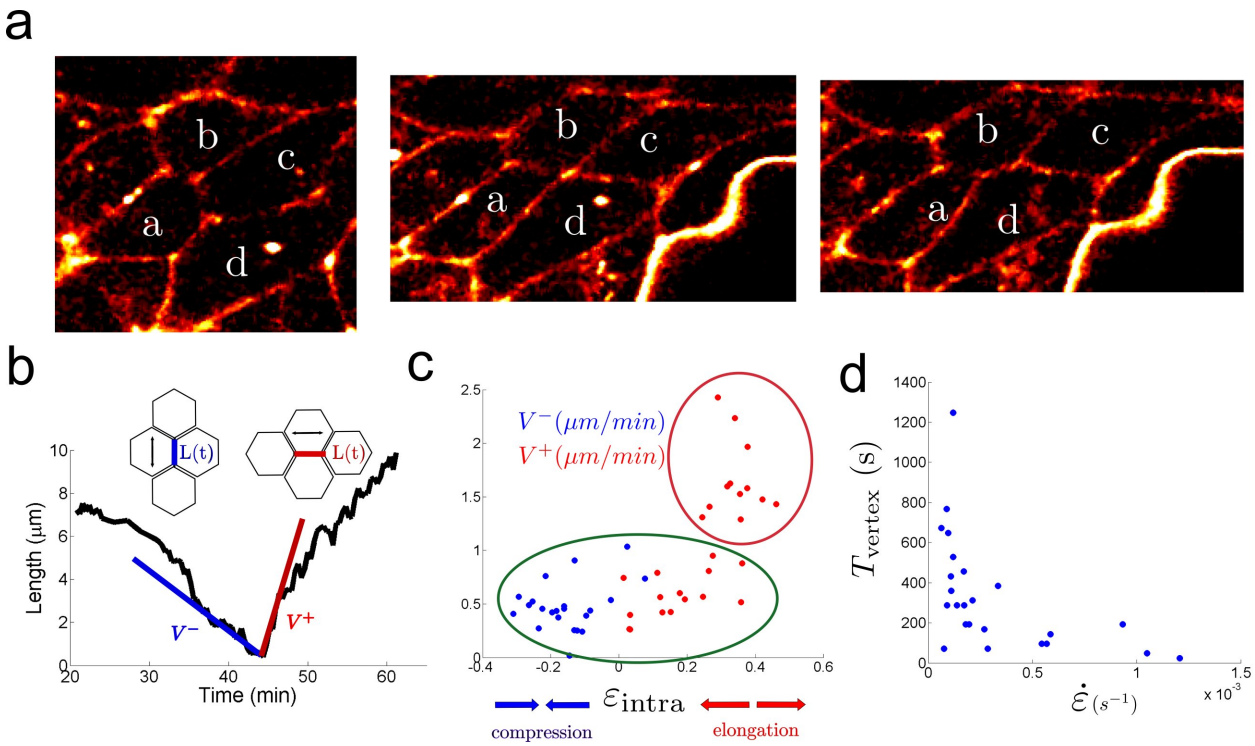

Figure 4: **Cell rearrangements.** (a) Typical cell rearrangement in the aspired aggregate. Before the rearrangement, cells a and c are in contact, this contact progressively disappeared till one gets to the four-fold vertex stage. After the rearrangement, a new contact between cells b and d has been created. (b) Junction length evolution during a rearrangement. Length of the disappearing junction (in blue) and of the newly created one (in red) versus time. The junction almost vanishes at the four-fold vertex stage (See Supplementary Movie 3). (c) Link shrinkage and growth. V^- versus $\varepsilon^-_{\text{cell}}$ (blue) and V^+ versus $\varepsilon^+_{\text{cell}}$ (red). (d) Stability of four-fold vertex. Time T_{vertex} where the junction that undergoes a rearrangement is below a cutoff length $L_{\text{small}} = 2\ \mu$m, versus $\dot{\varepsilon}_{\text{tot}}$.

To relate these quantities with the local cell deformation during the rearrangement, we project the tensor ε_{cell} on the direction of the junction that disappears / appears. It yields $\varepsilon^-_{cell} = \varepsilon_{cell}\cos(2\theta^-)$ where θ^- is the angle between the disappearing link and the principal direction (i.e. eigenvector corresponding to the positive eigenvalue) of ε_{cell}; and $\varepsilon^+_{cell} = \varepsilon_{cell}\cos(2\theta^+)$ where θ^+ is the angle between the appearing link and the principal direction of ε_{cell} (Fig 4c). We observe that the disappearing junction is compressed, and that the newly created junction is elongated, which is consistent with the fact that observed rearrangements are passive ones triggered by the mesoscopic flow imposed by the aspiration.

We plot V^+ and V^- versus ε^+_{cell} and ε^-_{cell}, that are averaged on the same time $T = 6$ min as the velocities in Fig. 4c. For $-0.3 < \varepsilon_{cell} < 0.3$, the velocities V^- and V^+ are around the mean value $\approx 0.5\ \mu$m/min. For $\varepsilon^+_{cell} > 0.3$, the mean value of V^+ increases suddenly up to $\approx 2.5\ \mu$m/min. We also looked at the life time T_{vertex} of a "four-fold vertex stage" (Fig. 4d). We define it as the stage where the cell-cell junction is below $2\ \mu$m, which is small compared to the cell size, and large enough to avoid artefacts due to the resolution on the length determination when the junction is small. We observe that the life time of a four-fold vertex at null deformation rate can be large, which is qualitatively different from the physics of liquid foams, where the four-fold vertex is unstable (30). The life-time of the four-fold vertex in a biological tissue could be related to the dynamics of adhesion remodeling (31, 32), i.e. the timescale necessary for non-contacting cells to create a new junction. At a high cell deformation but null deformation rate, we could imagine that the four-fold vertex lifetime is dominated by active fluctuations and adhesion remodeling. Conversely, at both high cell deformation and deformation rate, a new contact between cells can be created without maturing cell-cell adhesion (i.e. passive new contact and sliding of cells triggered by the mesoscopic deformation rate).

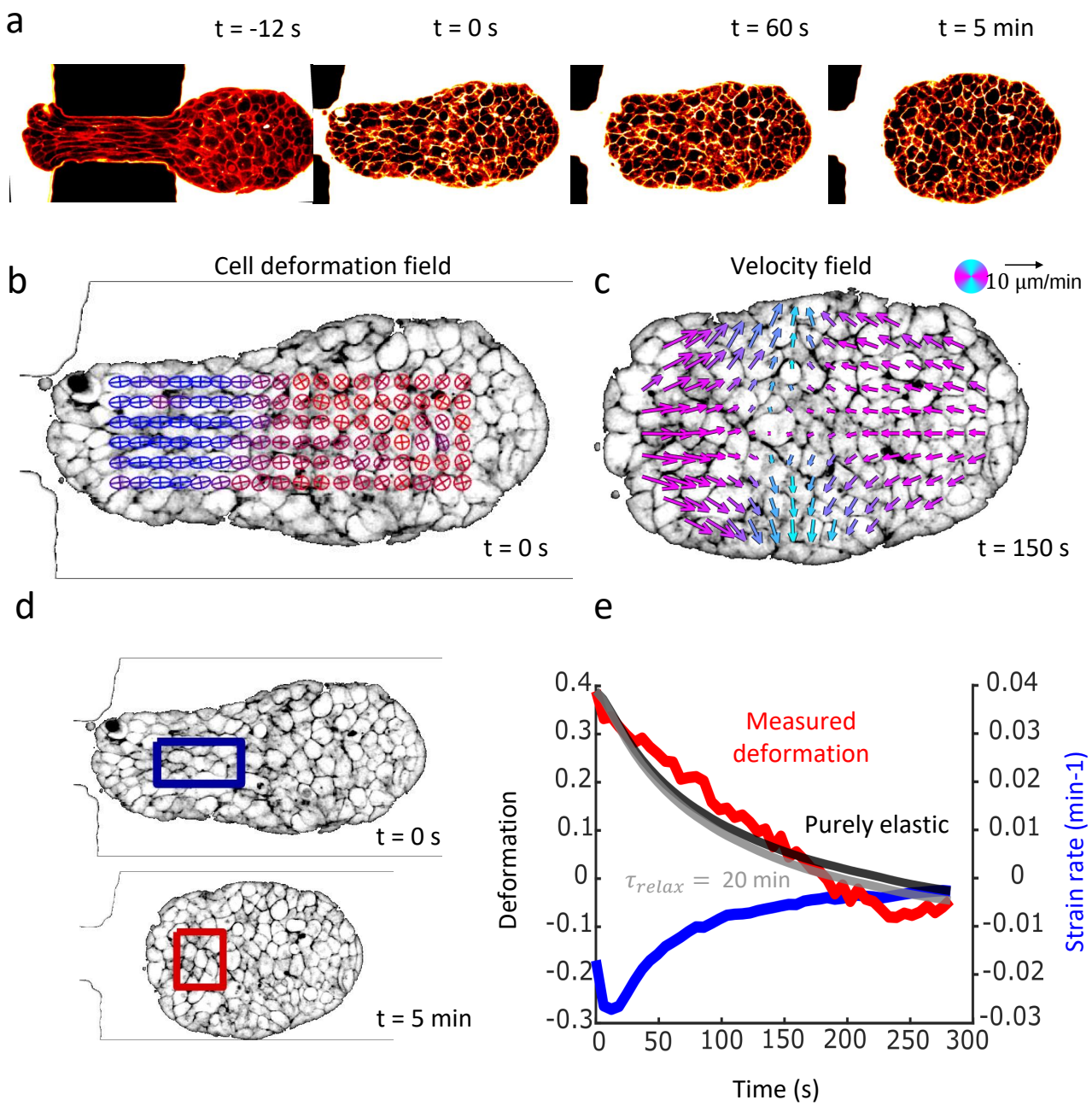

Figure 5: **Aggregate rapid relaxation.** (a) Typical aggregate during rapid relaxation phase. The aggregate is aspired in a short channel, the right part had time to slowly relax during the aspiration. When the radius of the remaining part of the aggregate to be aspired is of the same size than the channel size ($t = -12s$), the aggregate part still aspired within the channel relaxes quickly ($t = 0s$) until the aggregate reaches a symmetric shape ($t \approx 200s$) (See Supplementary Movie 4). (b) Inertia ellipses representative of cell anisotropy, which is color-coded from 1 (red) to 2 (blue). (c) Velocity field during the relaxation. (d) Virtual patch of tissue deformed and advected by the measured deformation rate/velocity field measured by optic flow (same method as in Fig. 3). (e) In blue, $\varepsilon_{\text{tot}}^{xx-yy}$, in red $\varepsilon_{\text{cell}}^{xx-yy}$, in black, simulated $\varepsilon_{\text{cell}}^{xx-yy}$ if there was no cell shape relaxation (purely elastic deformation), in gray, simulated $\varepsilon_{\text{cell}}^{xx-yy}$ in the case of a typical cell shape relaxation timescale τ_{relax}.

3.4 Aggregate relaxation after aspiration.

The aspired aggregate can either relax in a reservoir at the end of the channel or being pushed back in the entrance reservoir. In both cases, the relaxation is still an effective two-dimensional relaxation as the tissue is still confined in the z direction. The relaxation dynamics qualitatively depends on the time the tissue has spent in the channel, and two regimes can be distinguished.

During a rapid aspiration, cell rearrangements do not have time to occur and the aggregate deformation is uniquely due to cell deformation. In this case, the aggregate shape relaxation in a reservoir corresponds to a cell deformation relaxation on the minute timescale (Fig. 5). This corresponds to an effective visco-elastic solid behavior (Kelvin-Voigt) with a typical timescale of relaxation $\tau_{cell} \sim \frac{\eta_{\rm cell}}{G} \sim 50$ s; which, taking $G \sim 100$ Pa, yields: $\eta_{\rm cell} \sim 5000$ Pa.s.

If the aspired aggregate is kept in the channel for a long time ($T_{\rm aspi} > \tau_{\rm relax}$), the cell deformation has enough time to relax inside the channel through rearrangements (Fig. 6). In this case, when the aggregate starts to relax in the reservoir, the cells shape is already isotropic but we still observe a relaxation of the aggregate shape (Fig. 6a) associated with an elongation of cells along the perpendicular axis to the main axis of elongation of the aggregate. This phenomenon can be explained by the fact that tissue surface tension triggers a compaction of the aggregate along its main axis of elongation. Since cells can rearrange and relax their shape under stress on timescales $\tau_{\rm relax} \sim 20$ minutes, the surface tension related compression triggers significant cell deformations without any rearrangement on timescales shorter than $\tau_{\rm relax}$. This is the signature of an elastocapillar behavior for the tissue, which can happen when the aggregate surface tension Γ is high enough to trigger significant cell deformations $\varepsilon_{\rm cell} = \frac{\Gamma}{GR_{\rm ag}}$ with $R_{\rm ag}$ the typical curvature radius at the beginning of the rounding phases and G the effective Young modulus of the tissue. We assume here that the aggregate surface tension Γ does not change of order magnitude due to the aspiration. Taking $\Gamma = 5$ mN/m from our previous macroscopic experiments in F9 cells aggregates (33) and $R_{\rm ag} \sim R_{\rm channel}/2 \sim 25$ μm, we find $G \sim 100$ Pa, which is compatible with the result obtained in section "Cell deformations and rearrangements during aspiration".

4 Discussion

To recapitulate the different behaviors observed in the previous sections, we propose a rheological diagram of the aggregate combining the contributions of intra-cellular rheology (cell deformations), inter-cellular rheology (cell rearrangements) and aggregate surface tension (Fig. 7).

During the aspiration, the aggregate is partially elastically deformed in the channel and partially irreversibly deformed due to rearrangements. The balance between these two behaviors is governed by the Weissenberg number, which determines whether the flow displays more liquid or elastic characteristics. We can estimate $We = \dot{\varepsilon}\tau_{\rm relax} \sim 0.5$ in the aspiration and relaxation experiments (Fig. 3c, Fig. 5e, Fig. 6e). This Weissenberg number is of order of unity, which shows that in such experiments both tissue effective viscosity and elasticity play a comparable role, and that elasticity transport can not be neglected in the experiment analysis. High Weissenberg flows are probably relevant in fast morphogenetic changes phases like gastrulation, where tissues encounter both high strain rates and cell deformations.

Single-cell scale events such as rearrangements can be manually identified (Fig. 3d). When analyzing single rearrangement dynamics, the correlation between V^+, V^-, $T_{\rm vertex}$, $\dot{\varepsilon}$ and ε_{cell} gives insights about the microscopic origin of the cell deformation effective relaxation time $\tau_{\rm relax}$. We can estimate that $\tau_{\rm relax}$ scales like the creation time of a new junction with $\tau_{\rm relax}^{\rm micro} \approx \frac{L_{\rm cell}}{V^+} \approx 20$ min with $L_{\rm cell} = 10$ μm and $V^+ = 0.5$ μm/min. This estimation of $\tau_{\rm relax}^{\rm micro}$ is consistent with the value of $\tau_{\rm relax}$ estimated at the scale of the group of cells, in the section "Cell deformations and rearrangements during aspiration". However, we see that this relaxation time can decrease at the vicinity of the channel for two reasons: first $T_{\rm vertex}$ will be close to zero as the strain rate is high at the vicinity of the channel, second we can see that V^+ goes up to 2.5 μm/min when the cells are stretched by more than 30%. The flow rate at the vicinity of the channel is then probably dominated by a regime where cells slide on each other without having the time to create new adhesive junctions. This emphasizes a difficulty in pipet aspiration experiments as the measured effective tissue viscosity might reflect the physics of highly deformed tissues and non-quasistatic rearrangements near the channel entrance.

Cell rearrangement dynamics has been studied in *in vivo* systems like Drosophila (31, 32, 34, 35) or Xenopus embryos (36), *in vitro* tissues (28) and numerically for *in silico* tissues (37). However, in the context of embryo development or collective cell migration *in vitro*, it is difficult to uncouple the passive and active mechanisms in rearrangements. Here, we present an experimental system to characterize quantitatively the passive cell rearrangements triggered by an imposed flow.

5 Conclusion and perspectives

Our experimental system coupling a microfluidic constriction and two photon microscopy enables to impose heterogeneous tissue flows to 3D cell aggregates and quantify the tissue mechanical response at the cellular scale by controlling the force applied to the aggregate and the geometry of the tissue flow and simultaneously imaging at sub-cellular resolution cell contours.

3D cell aggregates are model systems of active fluctuating cellular materials. We propose here to measure tissue effective rheological parameters averaged on time and space. To go beyond and understand in detail how cell rearrangements dynamics

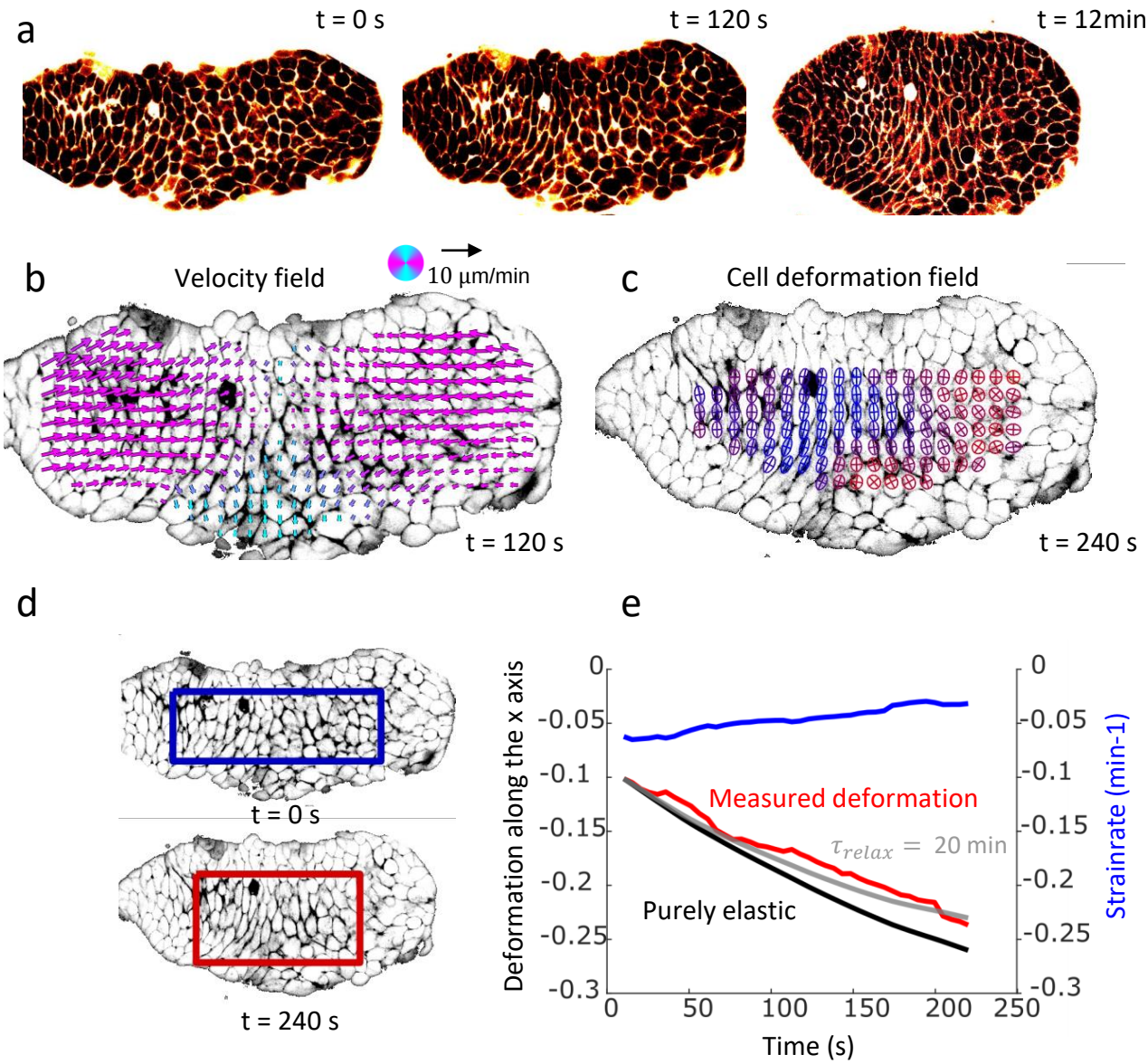

Figure 6: **Aggregate long-term relaxation** (same analysis and imaging methods as in Fig. 3). (a) Typical aggregate during long-term relaxation phase. The aggregate is aspired in a long channel. When the aggregate is released from the channel after a longer time spent in the channel (30 minutes), it undergoes first a rapid and partial shape relaxation similar to the one of Fig. 5 (See Supplementary Movie 5), associated with cell elongation relaxation along the x axis, and then continues to relax by compressing the cells along the x axis. (b) Velocity field corresponding to the compaction of the aggregate obtained with optic flow. (c) Inertia ellipses anisotropy is coded from 1, blue, to 2, red. (d) Virtual patch of tissue deformed and advected by the measured deformation rate/velocity field measured by optic flow (same method as in Fig. 3). (e) In blue, $\dot{\varepsilon}_{\mathrm{tot}}^{xx-yy}$, in red $\varepsilon_{\mathrm{cell}}^{xx-yy}$, in black, simulated $\varepsilon_{\mathrm{cell}}^{xx-yy}$ if there was no cell shape relaxation (purely elastic deformation), in green, simulated $\varepsilon_{\mathrm{cell}}^{xx-yy}$ in the case of a typical cell shape relaxation timescale τ_{relax}.

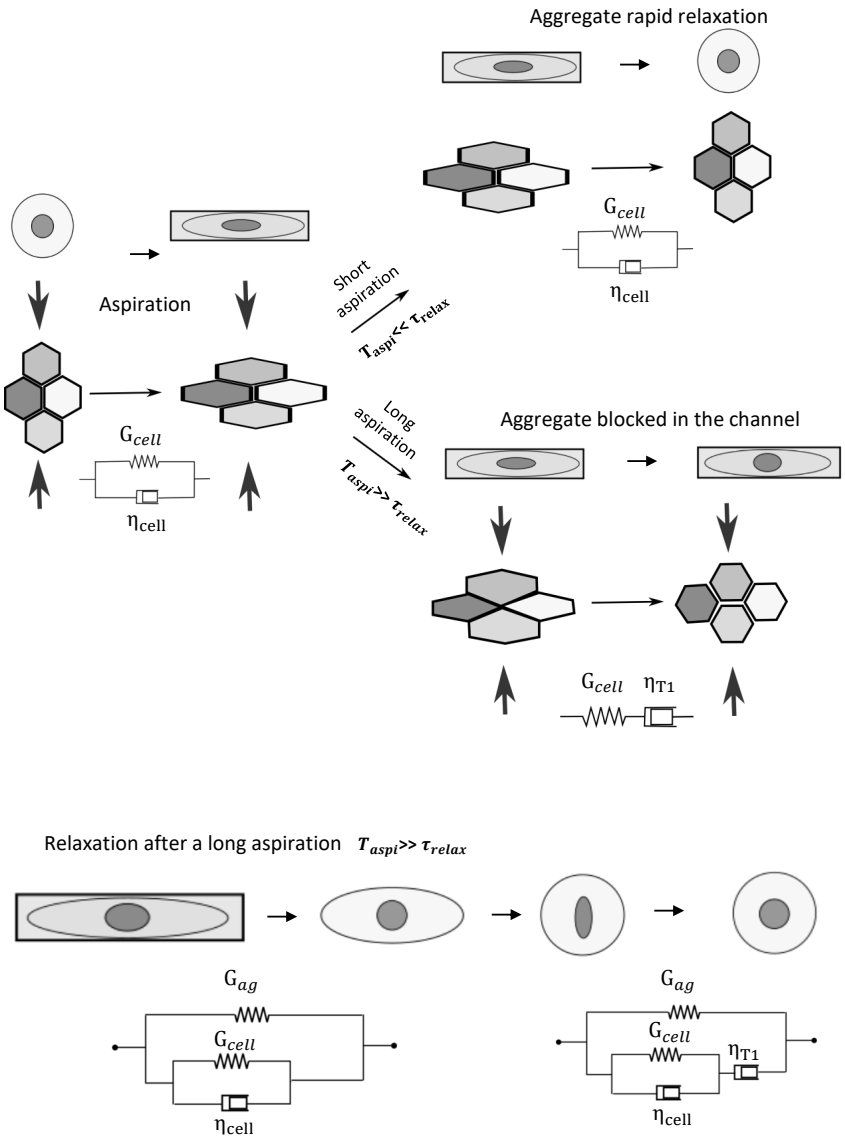

Figure 7: **Proposed rheological diagram for the aggregate.** (a) Cellular block without rearrangements: the cells can be described as a visco-elastic solid (Kelvin-Voigt) with a typical timescale of relaxation $\tau_{cell} \sim \frac{\eta_{\rm cell}}{G} \sim 50$ s which, taking $G \sim 100$ Pa, yields: $\eta_{\rm cell} \sim 5000$ Pa.s. (b) Rearrangements: the tissue composed of cells that can deform and rearrange can be at first order described as a visco-elastic liquid (Maxwell) with a typical timescale of relaxation of cell shape $\tau_{\rm relax} \sim \frac{\eta_{\rm T1}}{G} \sim 1000$ s which, using the value $G \sim 100$ Pa, yields $\eta_{\rm T1} \sim 100000$ Pa.s. (c) Schematic representation of what happens during an aspiration and a relaxation experiments depending whether the cell shape has time to relax due to cell rearrangements during the aspiration phase ($T_{\rm aspi}$ compared to $\tau_{\rm relax}$). (d) Schematic rheological diagram proposed for the while aggregate, with $G_{\rm ag}$ an effective elasticity at the aggregate level as the surface tension drives rounding of the aggregate.

is affected by the mechanical history of the tissue (to address questions such as : How long and how fast has the tissue been deformed? Were the cells deformed? When did they rearrange for the last time?), it could be useful to optimize both the geometry of the aspiration to trigger less abrupt cell transitions in cell deformation near the channel, and the cell segmentation and tracking methods (e.g based on Deep Neural Networks) to detect automatically cell rearrangements over many experiments to reach higher statistics.

In addition, the mechanical stress field is unknown inside aspired tissues: embedding deformable stress sensors inside the tissue (18, 38–40) would enable to relate cell deformation with the local tissue stress. We could also use cell segmentation to infer junctions tensions (41) and how they are modulated by cell deformations and rearrangements.

How cell membrane trafficking, adhesion proteins and molecular motors dynamics affect rearrangements dynamics and are relocalized during junction remodeling in 3D tissues is still not well understood. Combining our method with cell lines endowed with fluorescent reporters of such proteins would enable to quantify their dynamics using fluorescence recovery after photobleaching technics for example.

This microfluidic platform could also be a useful simple tool for perturbing mechanosensitive pathways by applying shear stresses and to quantify the effect on biomechanical networks (using fluorescent reporters or doing RNA sequencing afterwards, as it is easy to collect the aspired aggregates after the experiment). It could also be used to understand further the role of mechanics in development by accessing bulk tissue rheological properties heterogeneities (using systems such as gastruloids).

For these kind of applications, it could be useful to develop parallel and/or sequential aspiration was done for single cells experiments.

Supplementary Movies

Supplementary movies can be downloaded from the following link: https://doi.org/10.5281/zenodo.6360771
Supplementary Movie 1: 40 minutes long timelapse (brightfield) of an aggregate aspired in a channel.
Supplementary Movie 2: 60 minutes long timelapse (two-photon microscopy) of an aggregate aspired in a channel.
Supplementary Movie 3: cell-cell junctions involved in cellular rearrangements in Supplementary Movie 2.
Supplementary Movie 4: aspiration and rapid relaxation experiment (two-photon microscopy).
Supplementary Movie 5: relaxation experiment after a long aspiration (two-photon microscopy).

Acknowledgements

We thank the Nanoptec platform at ILM and especially Christophe Moulin, and the ImagoSeine core facility. We thank A. Nagafuchi for his generous gift of F9 cells, David Charalampous for developing the pressure control device, Alain Richert for help on tissue culture, Rémy Fulcrand for help on wafer fabrication in clean room, Pascal Hersen for letting us use his wet lab for microfluidic device preparation.

References

[1] C.P. Heisenberg, Y. Bellaïche, Cell **153**, 948 (2013)
[2] T. Takebe, J.M. Wells, Science (New York, N.Y.) **364**(6444), 956 (2019). . URL https://www.science.org http://www.ncbi.nlm.nih.gov/pubmed/31171692 http://www.pubmedcentral.nih.gov/articlerender.fcgi?artid=PMC8212787
[3] A.R. Harris, L. Peter, J. Bellis, B. Baum, A.J. Kabla, G.T. Charras, Proc. Natl. Acad. Sci. U.S.A. **109**(41), 16449 (2012). . URL http://www.ncbi.nlm.nih.gov/pubmed/22991459 http://www.pubmedcentral.nih.gov/articlerender.fcgi?artid=3478631&tool=pmcentrez&rendertype=abstract
[4] J.C.M. Mombach, D. Robert, F. Graner, G. Gillet, G.L. Thomas, M. Idiart, J.P. Rieu, Physica A: Statistical and Theoretical Physics (Amsterdam) **352**(2-4), 525 (2005). URL D:\helene\articles\rieu\mombach05.pdf
[5] P. Marmottant, A. Mgharbel, J. Käfer, B. Audren, J.P. Rieu, J. Vial, B. Van Der Sanden, A. Marée, F. Graner, H. Delanoë-Ayari, Proc. Natl. Acad. Sci. U.S.A. **106**(41), 17271 (2009). URL http://www.pnas.org/content/106/41/17271.short
[6] S. Grosser, J. Lippoldt, L. Oswald, M. Merkel, D.M. Sussman, F. Renner, P. Gottheil, E.W. Morawetz, T. Fuhs, X. Xie, S. Pawlizak, A.W. Fritsch, B. Wolf, L.C. Horn, S. Briest, B. Aktas, M.L. Manning, J.A. Käs, Physical Review X **11**(1), 011033 (2021). . URL https://journals.aps.org/prx/abstract/10.1103/PhysRevX.11.011033 https://link.aps.org/doi/10.1103/PhysRevX.11.011033
[7] P. Fernández, L. Heymann, A. Ott, N. Aksel, P.a. Pullarkat, New J. Phys. **9**(11), 419 (2007). . URL http://stacks.iop.org/1367-2630/9/i=11/a=419?key=crossref.0389492ca1f71a5ec419feee7b7dbc10
[8] T.V. Stirbat, Microscopic origin of the rheological and surface properties of embryonic cell aggregates. Ph.D. thesis, Université Lyon 1 (2013)
[9] K. Guevorkian, M.J. Colbert, M. Durth, S. Dufour, F. Brochard-Wyart, Phys. Rev. Lett. **104**(21), 1 (2010). . URL http://link.aps.org/doi/10.1103/PhysRevLett.104.218101

[10] M.S. Yousafzai, V. Yadav, S. Amiri, M. Staddon, A.P. Tabatabai, Y. Errami, G. Jaspard, S. Amiri, S. Banerjee, M.P. Murrell, bioRxiv (August), 2020.08.29.273334 (2020). URL https://www.biorxiv.org/content/10.1101/2020.08.29.273334v1

[11] F. Montel, M. Delarue, J. Elgeti, D. Vignjevic, G. Cappello, J. Prost, New J. Phys. **14**(5), 055008 (2012). . URL http://stacks.iop.org/1367-2630/14/i=5/a=055008?key=crossref.6f1deb67a78ab8f14b7762475ba2c7c4

[12] G. Mary, F. Mazuel, V. Nier, F. Fage, I. Nagle, L. Devaud, J.C. Bacri, S. Asnacios, A. Asnacios, C. Gay, P. Marcq, C. Wilhelm, M. Reffay, PREPRINT (Version 1) available at Research Square, DOI 10.21203/rs.3.rs-130138/v1 (2021)

[13] B. Guirao, S.U. Rigaud, F. Bosveld, A. Bailles, J. López-Gay, S. Ishihara, K. Sugimura, F. Graner, B. Y., eLife **4**, e08519/1 (2015)

[14] R. Etournay, M. Popović, M. Merkel, A. Nandi, C. Blasse, B. Aigouy, H. Brandl, G. Myers, G. Salbreux, F. Jülicher, S. Eaton, eLife **4**(JUNE2015) (2015). . URL https://elifesciences.org/articles/07090

[15] T.P.J. Wyatt, A.R. Harris, M. Lam, Q. Cheng, J. Bellis, A. Dimitracopoulos, A.J. Kabla, G.T. Charras, B. Baum, Proc. Natl. Acad. Sci. U.S.A. **112**(18), 5726 (2015)

[16] J. Fouchard, T.P.J. Wyatt, A. Proag, A. Lisica, N. Khalilgharibi, P. Recho, M. Suzanne, A. Kabla, G. Charras, Proceedings of the National Academy of Sciences **117**(17), 9377 (2020). . URL https://www.pnas.org/content/117/17/9377

[17] V. Du, N. Luciani, S. Richard, G. Mary, C. Gay, F. Mazuel, M. Reffay, P. Menasché, O. Agbulut, C. Wilhelm, Nature communications **8**(1), 400 (2017). . URL https://www.biorxiv.org/content/10.1101/2020.08.29.273334v1 https://www.biorxiv.org/content/10.1101/2020.08.29.273334v1.abstract http://www.ncbi.nlm.nih.gov/pubmed/28900152 http://www.pubmedcentral.nih.gov/articlerender.fcgi?artid=PMC5596024

[18] A. Mongera, P. Rowghanian, H.J. Gustafson, E. Shelton, D.A. Kealhofer, E.K. Carn, F. Serwane, A.A. Lucio, J. Giammona, O. Campàs, Nature **561**(7723), 401 (2018). . URL http://dx.doi.org/10.1038/s41586-018-0479-2

[19] R. David, O. Luu, E.W. Damm, J.W.H. Wen, M. Nagel, R. Winklbauer, Development (Cambridge, England) **141**(19), 3672 (2014). . URL http://www.ncbi.nlm.nih.gov/pubmed/25249459

[20] I. Regev, K. Guevorkian, O. Pourquie, L. Mahadevan, Development **in press** (2022). . URL https://www.biorxiv.org/content/10.1101/187443v1

[21] I. Cheddadi, P. Saramito, B. Dollet, C. Raufaste, F. Graner, Eur. Phys. J. E **34**, 1 (2011)

[22] I. Golovkova, L. Montel, E. Wandersman, T. Bertrand, A.M. Prevost, L.L. Pontani, Soft Matter **16**(13), 3294 (2020). . URL https://pubs.rsc.org/en/content/articlehtml/2020/sm/c9sm02343g https://pubs.rsc.org/en/content/articlelanding/2020/sm/c9sm02343g http://xlink.rsc.org/?DOI=C9SM02343G

[23] A. Nagafuchi, Y. Shirayoshi, K. Okazaki, K. Yasuda, M. Takeichi, Nature **329**(6137), 341 (1987). . URL http://www.ncbi.nlm.nih.gov/pubmed/3498123 http://view.ncbi.nlm.nih.gov/pubmed/3498123

[24] B.D. Lucas, T. Kanade, in Proceedings DARPA¡ mage Understanding Workshop (1981), pp. 121–130

[25] M. Durande, S. Tlili, T. Homan, B. Guirao, F. Graner, H. Delanoë-Ayari, Physical Review E **99**(6), 062401 (2019). . URL https://link.aps.org/doi/10.1103/PhysRevE.99.062401

[26] F. Graner, B. Dollet, C. Raufaste, P. Marmottant, Eur. Phys. J. E **25**(4), 349 (2008). . URL http://www.ncbi.nlm.nih.gov/pubmed/18446271

[27] S. Tlili, C. Gay, F. Graner, P. Marcq, F. Molino, P. Saramito, Eur. Phys. J. E **38**, 33/1 (2015).

[28] S. Tlili, M. Durande, C. Gay, B. Ladoux, F. Graner, H. Delanoë-Ayari, Physical Review Letters **125**(8), 88102 (2020). . URL https://doi.org/10.1103/PhysRevLett.125.088102

[29] J.E. Perez, F. Fage, D. Pereira, A. Abou-Hassan, S. Asnacios, A. Asnacios, C. Wilhelm, Journal of Nanobiotechnology **19**(1), 117 (2021). . URL https://link.springer.com/articles/10.1186/s12951-021-00790-y https://link.springer.com/article/10.1186/s12951-021-00790-y https://jnanobiotechnology.biomedcentral.com/articles/10.1186/s12951-021-00790-y

[30] I. Cantat, S. Cohen-Addad, F. Elias, F. Graner, R. Höhler, O. Pitois, F. Rouyer, A. Saint-Jalmes, Foams: structure and dynamics (Oxford University Press, ed. S.J. Cox, 2013)

[31] P. Bardet, B. Guirao, C. Paoletti, F. Serman, V. Léopold, F. Bosveld, Y. Goya, V. Mirouse, F. Graner, Y. Bellaïche, Dev. Cell **5**, 534 (2013)

[32] B. Guirao, Y. Bellaïche, Current Opinion in Cell Biology **48**, 113 (2017). . URL https://linkinghub.elsevier.com/retrieve/pii/S0955067417300492

[33] T.V. Stirbat, A. Mgharbel, S. Bodennec, K. Ferri, H.C. Mertani, J.P. Rieu, H. Delanoë-Ayari, PLoS One **8**(2), e52554 (2013). . URL http://www.pubmedcentral.nih.gov/articlerender.fcgi?artid=3563668&tool=pmcentrez&rendertype=abstract

[34] M. Rauzi, P. Verant, T. Lecuit, P.F. Lenne, Nat. Cell Biol. **10**(12), 1401 (2008). . URL http://www.ncbi.nlm.nih.gov/pubmed/18978783

[35] R. Etournay, M. Popovic, M. Merkel, A. Nandi, C. Blasse, B. Aigouy, H. Brandl, G. Myers, G. Salbreux, F. Jülicher, S. Eaton, eLife **10.7554/eLife.07090** (2015)

[36] R. David, O. Luu, E.W. Damm, J.W.H. Wen, M. Nagel, R. Winklbauer, Development **141**, 1 (2014)

[37] D. Bi, J.H. Lopez, J.M. Schwarz, M.L. Manning, Soft Matter **10**, 1885 (2014)

[38] O. Campàs, T. Mammoto, S. Hasso, R.A. Sperling, D. O'Connell, A.G. Bischof, R. Maas, D.A. Weitz, L. Mahadevan, D.E. Ingber, Nat. Methods **11**, 183 (2014)

[39] M.E. Dolega, M. Delarue, F. Ingremeau, J. Prost, A. Delon, G. Cappello, Nature Communications **8**(1), 14056 (2017). . URL https://www.nature.com/articles/ncomms14056 http://www.nature.com/articles/ncomms14056

[40] A. Souchaud, A. Boutillon, G. Charron, A. Asnacios, C. Noûs, N.B. David, F. Graner, F. Gallet, Development **149**, 199765/1 (2022).

[41] G.W. Brodland, J.H. Veldhuis, S. Kim, M. Perrone, D. Mashburn, M.S. Hutson, PLoS One **9**(6), e99116 (2014). . URL

http://www.pubmedcentral.nih.gov/articlerender.fcgi?artid=4055627&tool=pmcentrez&rendertype=abstract